Corrosion-induced cracking in LC3 and OPC mortars: influence of binder type and mechanical properties

Citation for the original published paper (version of record):
Felix, T., Baba Ahmadi, A., Dijkstra, J. et al (2026). Corrosion-induced cracking in LC3 and OPC mortars: influence of binder type and mechanical properties. Materials and Structures/Materiaux et Constructions, 59(7).
http://dx.doi.org/10.1617/s11527-026-03224-z

Materials and Structures (2026) 59:334
https://doi.org/10.1617/s11527-026-03224-z

ORIGINAL ARTICLE

Corrosion-induced cracking in LC^3 and OPC mortars: influence of binder type and mechanical properties

Talles Felix · Arezou Babaahmadi · Jelke Dijkstra · Karin Lundgren

Received: 2 March 2026 / Revised: 17 July 2026 / Accepted: 24 July 2026

Abstract Limestone calcined clay cement (LC^3) is a promising low- CO_2 alternative to ordinary Portland cement (OPC), but its long-term performance with respect to corrosion-induced cracking in reinforced concrete remains poorly understood. This study investigates the interplay between binder type, material properties, and corrosion-induced cracking in steel-reinforced mortars made with OPC and LC^3. Accelerated corrosion experiments were conducted using the impressed current technique, and the time-to-cracking was determined from electrical potential measurements to assess the corrosion level leading to matrix cracking. LC^3 mortars exhibited cracking at lower corrosion levels compared with OPC mortars, indicating a lower resistance to corrosion-induced mechanical stresses. This behavior could be correlated to fracture energy, which was lower in the LC^3 systems. Although LC^3 mortars showed superior resistance to chloride ingress, their reduced fracture performance suggests a potential trade-off. These findings highlight that durability assessments may benefit from considering both transport and fracture-related properties.

Keywords Limestone calcined clay cement (LC^3) · Corrosion-induced cracking · Reinforcement corrosion · Long-term performance · Fracture energy · LC^3 durability

1 Introduction

Currently, major research efforts are invested in developing low-carbon composite binders, in which Supplementary Cementitious Materials (SCMs) partially replace clinker. Calcined clays are one example [1, 2], which can also be combined with other SCMs to form ternary binders and increase clinker replacement, with limestone being a particularly effective synergistic addition [3–6]. This led to the development of Limestone Calcined Clay Cement (LC^3), which has emerged as a promising low-carbon alternative to Ordinary Portland Cement (OPC), enabling up to 40% reductions in CO_2 emissions while delivering comparable or higher mechanical performance [7–9].

Arezou Babaahmadi, Jelke Dijkstra and Karin Lundgren have contributed equally to this work.

T. Felix · A. Babaahmadi · J. Dijkstra · K. Lundgren
Department of Architecture and Civil Engineering, Chalmers University of Technology, Gothenburg, Sweden

A. Babaahmadi
e-mail: arezou.ahmadi@chalmers.se

J. Dijkstra
e-mail: jelke.dijkstra@chalmers.se

K. Lundgren
e-mail: karin.lundgren@chalmers.se

T. Felix (✉) · K. Lundgren
Wallenberg Initiative Materials Science for Sustainability, Chalmers University of Technology, Gothenburg, Sweden
e-mail: talles.felix@chalmers.se

Published online: 06 August 2026

However, durability remains a critical concern for novel binders. In civil engineering applications, structures are typically designed for service lives of 50–100 years, and demonstrating long-term performance is essential. Steel reinforcement is vital for structural performance, and corrosion of embedded steel is a major cause of degradation in existing infrastructure. This is particularly critical in chloride-rich environments, such as coastal regions and areas exposed to de-icing salts, where chlorides can depassivate the protective layer of steel and initiate corrosion [10]. Uncracked concrete and mortars containing SCMs generally exhibit superior resistance to chloride ingress compared to OPC systems [11, 12], and this is especially evident for LC^3 binders [13, 14].

Nevertheless, corrosion is predetermined to happen over long service periods. In practice at the engineering scale, concrete inevitably cracks due to restraint, shrinkage, creep, freeze-thaw cycles, and mechanical loading [15]. These cracks can act as preferential pathways for chloride ingress [15–17], accelerating reinforcement corrosion, reducing the steel cross-section, and causing volumetric expansion of corrosion products that ultimately leads to concrete spalling [18]. Although LC^3 has attracted considerable interest as a low-CO_2 alternative to OPC, its performance under corrosion-induced cracking remains poorly understood. Thus, the present work presents an essential first step to close this knowledge gap.

This study investigates corrosion-induced cracking in steel-reinforced mortars containing LC^3, in comparison with OPC-based mortars. The primary objective is to determine the corrosion level required to initiate matrix cracking, for varying concrete qualities. This was assessed by estimating the time-to-cracking, t_{crack}, from electrical potential measurements during impressed current corrosion tests. The measured t_{crack} values were subsequently correlated with key mechanical and transport properties, namely compressive strength f_c, tensile strength f_t, fracture energy G_F, and the non-steady-state chloride migration coefficient D_{nssm}. By studying these correlations, this work aims to clarify whether LC^3 mortars respond differently to corrosion-induced stresses compared with OPC mortars, and whether such responses can be predicted from measurable material properties.

2 Methods and materials

An impressed current test was used to accelerate steel corrosion and determine the time-to-cracking, t_{crack}, in OPC and LC^3 mortars. Additional experiments were performed to characterize their mechanical and transport properties, to further interpret the corrosion test results. Uniaxial compression tests were conducted to determine the compressive strength f_c, wedge-splitting tests were performed to obtain the tensile strength f_t and fracture energy G_F, and the non-steady-state migration test was employed to measure the chloride migration coefficient D_{nssm}. These properties were subsequently correlated with t_{crack}.

2.1 Materials and specimen preparation

A total of four distinct mortar mixes were prepared. Two of these mixes utilized OPC, while the other two employed LC^3. Within each binder type, a higher-strength and a lower-strength mortar were produced by varying specific mix parameters, designated as higher-strength OPC (H-OPC), lower-strength OPC (L-OPC), higher-strength LC^3 (H-LC^3), and lower-strength LC^3 (L-LC^3).

The 28-day compressive strength was used in this study as the starting point for mix design. Here, this property was tailored by varying the water/binder (w/b) ratio, in the case of the OPC mortars, or using either a higher- or lower-reactive metakaolin, in the case of the LC^3 mixes. This approach produced higher- and lower-strength variants for each binder type. The detailed compositions of these mixes are provided in Table 1.

The mixing procedure of the H- and L-OPC mortars involved the initial homogenization of solid components, followed by the gradual addition of water to achieve the target w/b ratio. A superplasticizer was incorporated into the H-OPC mix to enhance the workability of the fresh mortar. After mixing, the mortar was cast into molds, vibrated for compaction, and its surface was covered with polyethylene wrap to prevent moisture loss. The specimens were demolded the following day, re-wetted, and wrapped in plastic film for a 28-day curing period prior to testing.

The LC^3 binders used for the H-LC^3 and L-LC^3 samples were prepared in the laboratory following the binder design proposed by Cheng et al. [20]. The

Table 1 Mix proportions of the mortars (mass per cubic meter and percentage by binder weight)

OPC: ordinary Portland cement, PP : PowerPozz™ metakaolin, MK: Metaver® K metakaolin, QZ: quartz powder, LS: limestone, GP: gypsum. [19][1] CEM I 52.5 R [38] was used as OPC. [2]Crushed-stone sand with particle size ranging 0–4 mm

	H-OPC		L-OPC		H-LC^3		L-LC^3	
Material	kg/m^3	%bw	kg/m^3	%bw	kg/m^3	%bw	kg/m^3	%bw
OPC[1]	480	100	457	100	236	50	236	50
PP	0	0	0	0	106.2	22.5	0	0
MK	0	0	0	0	0	0	106.2	22.5
QZ	0	0	0	0	35.4	7.5	35.4	7.5
LS	0	0	0	0	70.8	15	70.8	15
GP	0	0	0	0	23.6	5	23.6	5
Water	240	-	274.2	-	236	-	236	-
Sand[2]	1500	-	1428.1	-	1475	-	1475	-

primary difference between the H-LC^3 and L-LC^3 mixtures lay in the type of calcined clay used. In both cases, the calcined clay consisted of 75% commercial metakaolin and 25% quartz powder by weight. However, different metakaolins were employed: H-LC^3 incorporated PowerPozz™, whereas L-LC^3 used Metaver® K. Metaver® K was a less reactive metakaolin, suitable for a lower-strength LC^3 mortar. The H-LC^3 and L-LC^3 mortars were cast following the same procedure as the H-OPC sample.

2.2 Corrosion test

2.2.1 Specimen geometry

For the corrosion test, four cylindrical specimens were cast for each mortar type, with a central plain steel rod embedded in each. The rebar was positioned to ensure a 10 mm mortar cover on the sides and bottom. The upper part of the rebar protruded from the mortar surface and was threaded to facilitate the connection of electrical cables. The specimen geometry is detailed in Fig. 1.

2.2.2 Impressed current method

Corrosion of the steel rebars was accelerated using the impressed current method [21, 22]. The experimental setup is shown in Fig. 2. Each specimen was placed in a separate plastic container filled with a 5 wt% sodium chloride aqueous solution up to the height of the specimen, as indicated in Section A-A (Fig. 2). A copper mesh was placed in the solution-filled container surrounding each specimen. The positive terminal was connected to the steel reinforcement (anode) and the negative terminal to the copper mesh (cathode). Four specimens were simultaneously connected in series. The current *I* was provided by a custom-made current board that was connected to a Thurlby Thundar Instruments PL330

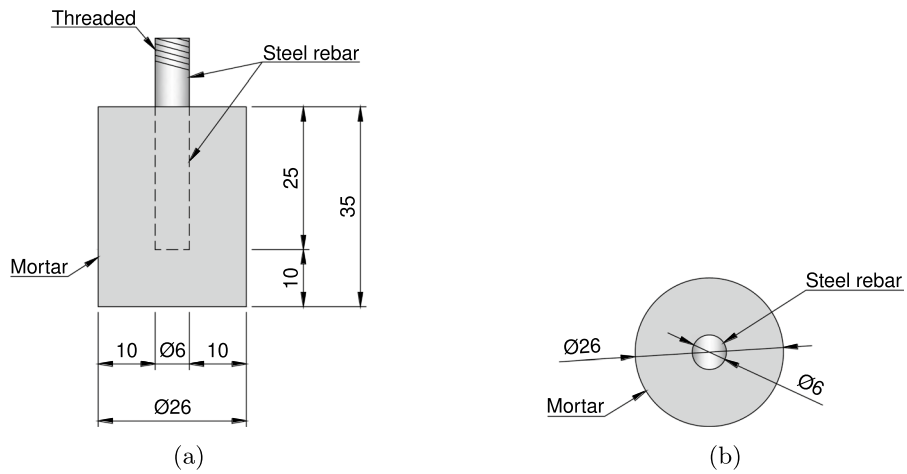

Fig. 1 Side view (**a**) and top view (**b**) of the corrosion test specimens with the reinforcement layout (dimensions in mm)

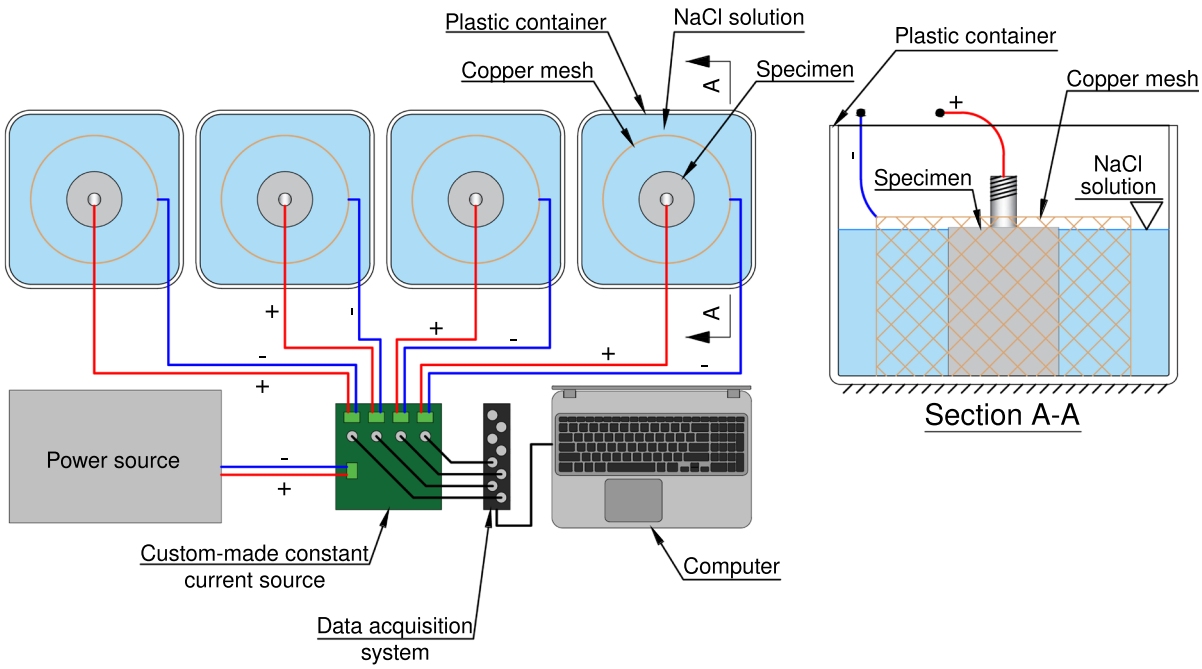

Fig. 2 Experimental setup for the impressed current corrosion test, including electrical circuit, specimen arrangement, and a section of the plastic container

DC power supply. The current board was designed to maintain the current flow constant by automatically adjusting the electrical potential. A current density $I_{corr} = 50$ µA/cm^2 was applied, a value considered appropriate to mimic natural corrosion [23]. Nevertheless, it is important to emphasize that the objective of the present study was not to reproduce natural corrosion, but to compare LC^3 and OPC mortars under the same accelerated corrosion protocol and under carefully controlled experimental conditions.

An IOLITE® data acquisition system was used along with the DewesoftX software to continuously monitor the electrical potential U in each specimen at a frequency of 120 measurements per hour. It should be noted that the primary objective of the potential measurements was to identify the onset of a sustained negative change in potential ΔU over consecutive intervals, from which t_{crack} of each specimen could be estimated. This potential drop is considered a reliable indicator that corrosion-induced cracks have reached the specimen surface. A recent study reported a significant increase in iron-57 concentration in the salt solution shortly after this drop is detected [24].

In the present study, the potential drop corresponding to t_{crack} was identified visually with a temporal resolution of 15 min. Derivative-based criteria, such as the minimum curvature of the potential-time curve, were also evaluated. However, due to the high temporal resolution of the measurements and the increasing noise level, particularly after cracking, the resulting second-derivative signals were dominated by numerical spikes during the abrupt potential collapse, preventing the reliable identification of a unique curvature minimum.

It should also be noted that the absolute values of t_{crack} obtained under impressed current conditions are influenced by the specific test methodology. Nevertheless, under constant current conditions, t_{crack} provides a meaningful indication of the corrosion level required to induce cracking, as it is directly related to the corrosion level according to Faraday's law.

2.3 Mechanical testing

2.3.1 Compressive strength test

The compressive strength f_c of the hardened mortar samples was determined in accordance with the

EN 12,390-3:2019 standard [25]. Three 100 × 100 × 100 mm^3 cubic specimens of each mortar were loaded to failure in a compression testing machine. The maximum compressive load $F_{c_{max}}$ sustained by each specimen was recorded, from which f_c was calculated. Unfortunately, a problem with the software caused the data loss of two of the three L-OPC specimens. Thus, the results of only one specimen are reported here for this specific mortar.

2.3.2 *The wedge splitting test*

The wedge splitting test was performed on three specimens of each mortar to determine their fracture energy G_F and the indirect tensile strength f_t, following the methodology proposed by Brühwiler [19]. Cubic specimens measuring 100 × 100 × 100 mm^3 were cast with a pre-formed groove on one face. A starter notch was sawn at the base of the groove after curing to define the crack ligament. The specimen geometry is illustrated in Fig. 3.

During the test, a pair of loading rollers was positioned within the groove, and a 15° wedge was driven vertically between them. This action transformed the vertical load F_V applied by the testing machine into a horizontal splitting force F_S, which induced a stable, Mode I crack propagation through the ligament. F_V and the crack mouth opening displacement (CMOD) were recorded at each displacement increment. F_S was calculated from F_V and the known wedge angle α using Eq. 1.

$$F_S = \frac{F_V}{2\tan\alpha} \tag{1}$$

Subsequently, the work required to split the specimen was quantified by integrating the area under the F_S -CMOD-curve. It was then normalized by the ligament area A_L to yield G_F, expressed as the energy dissipated per unit area of the fractured surface. Here, G_F is determined as an intrinsic material property under stable Mode I crack propagation. Consequently, G_F is suitable for comparing the relative crack propagation independently of geometry.

Furthermore, f_t was indirectly determined from the maximum splitting force $F_{S_{max}}$ using Navier's formula

$$f_t = \frac{F_{S_{max}}}{A_L} + \frac{F_{S_{max}} e}{I_L} z \tag{2}$$

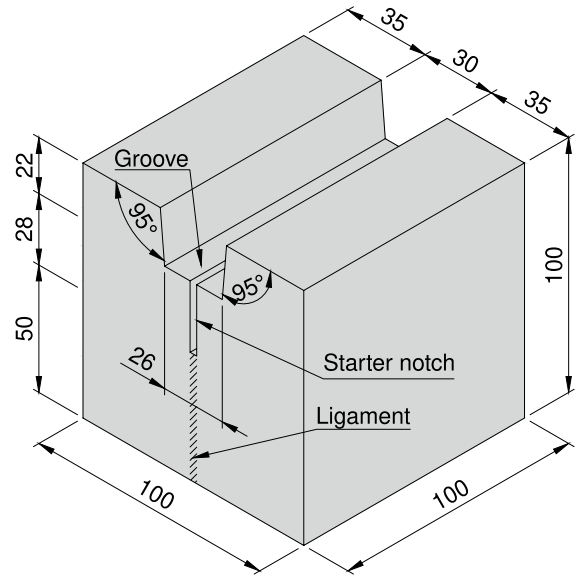

Fig. 3 Geometry of the wedge splitting test specimens. Dimensions are given in mm

where e was the distance from the point where $F_{S_{max}}$ was applied to the center of gravity of the ligament's cross-section, I_L was the cross-sectional moment of inertia of the ligament, and z was the distance from the center of gravity to the top of the ligament where the maximum tensile stress occurs and crack initiation is expected.

2.4 Non-steady-state migration experiment

The transport properties of the mortars were evaluated using the non-steady-state migration experiment, with the chloride migration coefficient D_{nssm} estimated according to the NT BUILD 492 method, also known as the Rapid Chloride Migration (RCM) test [26]. This test measures the resistance of mortars and concrete to chloride ion penetration. The samples were first saturated with water and then submitted to an external electrical potential, which accelerated the migration of chloride ions from an external sodium chloride aqueous solution into the specimens. Three specimens of each mortar were tested.

Following the specified test duration, the specimens were axially split, and the depth of chloride penetration was determined by spraying the freshly fractured surface with a silver nitrate solution. The presence of chlorides resulted in a visible color

change, and the penetration depth was measured at multiple points and averaged. D_{nssm} [$\times 10^{-12}$ m^2/s] could then be calculated based on this average value of the penetration depth x_d in meters, the absolute value of the applied voltage U in volts, test duration t in hours, specimen thickness L in millimeters, and the average value T of the initial and final temperatures in the anolyte solution in degrees Celsius, as shown in Eq. 3 [26].

$$D_{nssm} = \frac{0.0239(273+T)L}{(U-2)t}\left(x_d - 0.0238\sqrt{\frac{(273+T)Lx_d}{U-2}}\right) \quad (3)$$

3 Results

3.1 Material properties

The material properties evaluated in this study are plotted in Fig. 4. These include compressive strength f_c, tensile strength f_t, fracture energy G_F, and chloride migration coefficient D_{nssm}. Combined, these properties provide insight into both the mechanical performance and transport characteristics of the mortars, enabling a comprehensive comparison between OPC and LC^3 systems.

3.1.1 Compressive strength

As shown in Fig. 4a, higher-strength mortars exhibited similar compressive strengths: 63.1 MPa for H-OPC and 66.9 MPa for H-LC^3, with LC^3 slightly outperforming OPC. These results are consistent with previous studies reporting comparable or superior performance of LC^3 systems with similar kaolinite content [27, 28]. For lower-strength mortars, strengths of 49.8 MPa (L-OPC) and 40.2 MPa (L-LC^3) were achieved, confirming the intended differentiation in compressive strength.

3.1.2 Tensile strength

Tensile strength results, obtained via wedge-splitting tests, are presented in Fig. 4b. OPC mortars showed minimal variation. H-LC^3 exhibited a slightly higher value, whereas L-LC^3 displayed a marked reduction, suggesting that binder reactivity influences tensile capacity.

3.1.3 Fracture energy

The average F_S-CMOD curves of each mortar, from which the fracture energies were derived, are shown in Fig. 5. The post-peak behavior of the mortars containing LC^3 indicates a reduced ability to dissipate energy after crack initiation compared to the OPC-based systems. In particular, the H-LC^3 mortar exhibited a markedly more brittle response during the wedge splitting test, which made it difficult to capture its post-peak behavior reliably. Beyond a CMOD of approximately 0.05 mm, a sudden drop in the splitting force occurred simultaneously with an increase in CMOD. This response limited the ability to capture a smooth post-peak curve in this region, which is therefore represented by a dashed line. In addition, the standard deviation was higher than usual in this interval. As a result, the fracture energy of the H-LC^3 mortar was most likely overestimated to some degree. Nevertheless, it remains a reasonable approximation for the purposes of this study.

The fracture energy results indicate that this property is more strongly influenced by the binder type than by mechanical performance under compression or tension (Fig. 4c). The brittle post-peak response of the H-LC^3 mortar, for example, resulted in a significantly lower fracture energy compared to both H- and L-OPC mortars, despite its superior strength performance. This effect was even more pronounced for the L-LC^3 mortar, which exhibited a fracture energy approximately half that of the H-OPC mortar.

In the case of L-LC^3, the lower tensile strength also contributed to the reduced fracture energy. As shown in Fig. 5, the elastic response of all mortars was similar, as evidenced by the comparable initial linear portions of the F_S-CMOD curves. Consequently, the peak of the curve for the L-LC^3 mortar occurred at both a lower splitting force and a lower CMOD than for the other mortars, indicating that less energy was required to initiate cracking. Combined with the reduced post-cracking energy dissipation, this resulted in a smaller area under the F_S-CMOD curve and, therefore, in the lowest fracture energy among all mortars.

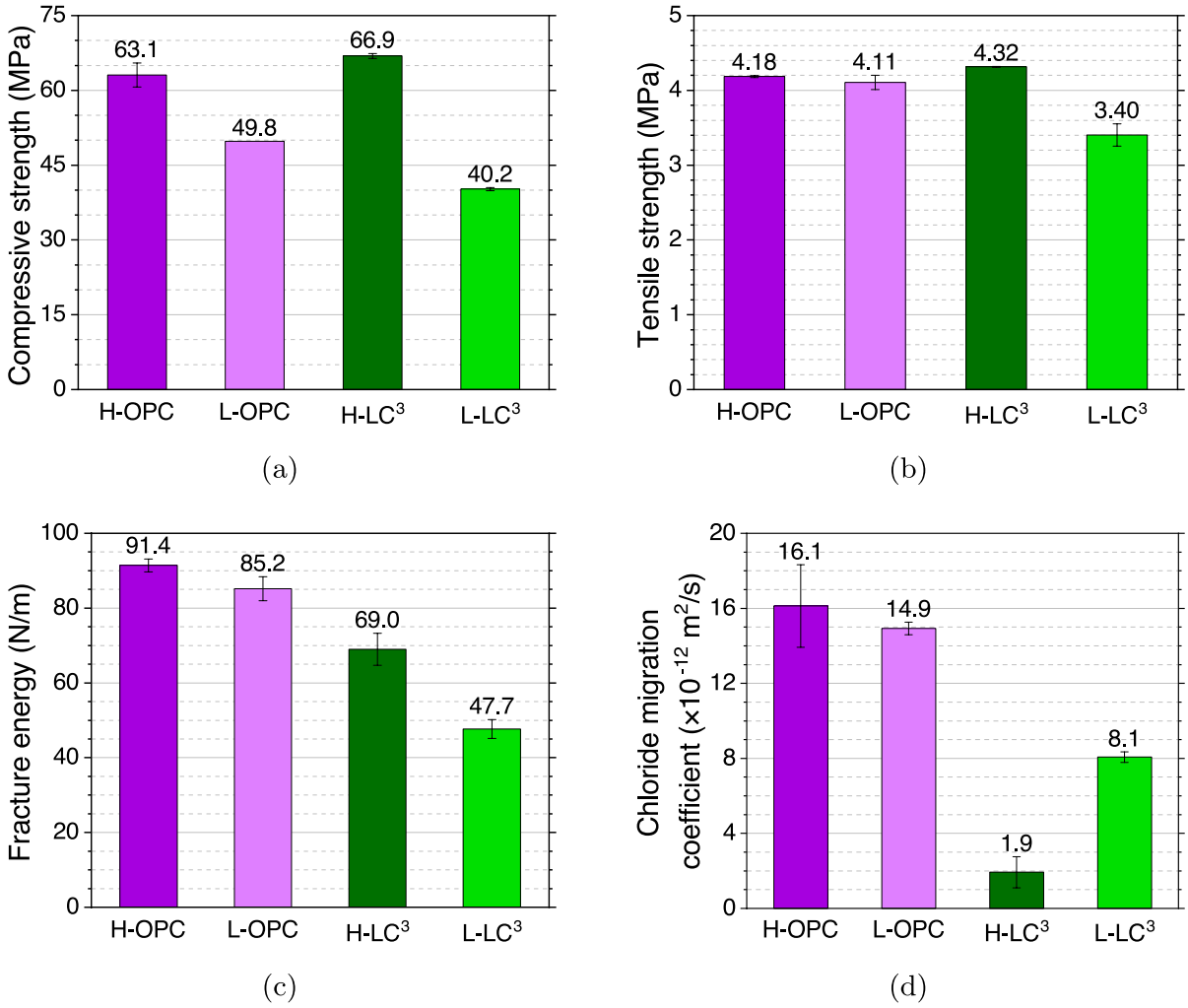

Fig. 4 Material properties of the higher-strength ordinary Portland cement (H-OPC), lower-strength ordinary Portland cement (L-OPC), higher-strength limestone calcined clay cement (H-LC^3), and lower-strength limestone calcined clay cement (L-LC^3) mortars after 28 days of curing: **a** compressive strength, **b** tensile strength, **c** fracture energy, and **d** chloride migration coefficient. Error bars indicate the standard deviations

3.1.4 Chloride migration coefficient

The influence of binder type on transport properties was assessed through the chloride migration coefficient D_{nssm} (Fig. 4d). Both H- and L-LC^3 mortars exhibited significantly lower D_{nssm} values compared to their OPC counterparts. Furthermore, it can be noted that the H- and L-OPC mortars showed D_{nssm} values within the same range when considering the associated standard deviations. Notably, the D_{nssm} value of H-LC^3 was approximately eight times lower than that of the OPC mortars, which is in good agreement with previously reported findings [14]. Moreover, the L-LC^3 mortar exhibited a D_{nssm} value approximately half of those of both OPC systems, corroborating the beneficial effect of LC^3 binders on chloride transport resistance.

3.2 Corrosion-induced cracking

The results of the corrosion test are presented in Fig. 6, which shows the time evolution of the

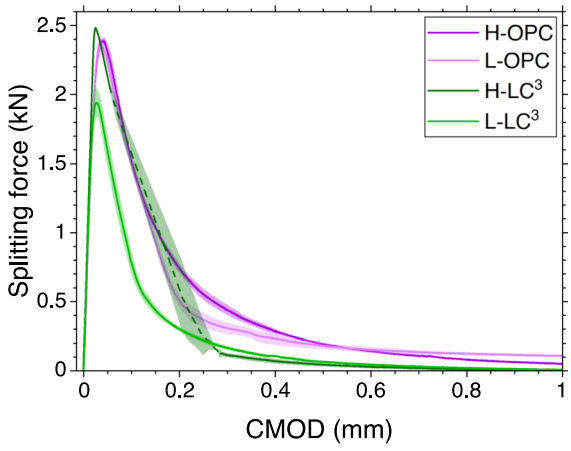

Fig. 5 Averaged splitting force (F_S) versus crack mouth opening displacement (CMOD) curves obtained from wedge splitting tests for the different mortars. The shaded regions indicate the standard deviation among specimens. Dashed segments denote regions where post-peak behavior could not be captured reliably due to brittle fracture

electrical potential U of each specimen. Four specimens were tested for each mortar type, and therefore four curves are shown in each plot, except for the L-OPC mortar. One L-OPC specimen was excluded from the analysis because corrosion products escaped from the top of the specimen. Leakage of corrosion products can reduce internal pressure on the concrete cover, preventing the development of surface cracks [29].

The corrosion level leading to cracking was assessed by the parameter t_{crack}, defined as the time at which a pronounced drop in electrical potential is observed. Each specimen's t_{crack} value was identified, and the mean values for each mortar type are reported in Table 2. These values are also indicated in the individual potential-time curves shown in Fig. 6. In addition, the potential-t_{crack} curves for each mortar were averaged, normalized, and plotted in Fig. 7 to facilitate comparison between the different systems. The final condition of the specimens after the corrosion experiment is exemplified in Fig. 8 with the L-LC^3-4 specimen.

The t_{crack} results followed the same trend observed for the fracture energy G_F. Both H- and L-OPC mortars exhibited higher t_{crack} values than the H- and L-LC^3 mortars. This indicates that mortars produced with LC^3 reached surface cracking at lower corrosion levels than the OPC systems, implying that less corrosion was required to initiate and propagate cracking in these materials.

Furthermore, the H-LC^3 specimens exhibited substantially higher measured potentials than the H-OPC, L-OPC, and L-LC^3 specimens, with pre-cracking values approximately four to six times higher. This behavior indicates a greater overall resistance of the LC^3 system to the imposed electrochemical process, which may be associated with factors such as its finer pore structure, lower pore solution conductivity, and differences in electrochemical reactions at the steel–mortar interface [30, 31].

In addition, the H-LC^3 specimens exhibited an initial increase in electrical potential followed by a gradual decrease prior to the drop evaluated as surface cracking, in contrast to the potential profiles of the other mortars (Fig. 6). This behavior might be related to the refined and highly tortuous pore structure of LC^3 systems, combined with reduced ionic conductivity of the pore solution resulting from pozzolanic reactions and the surface characteristics of calcined clays, which influence ionic transport under impressed current conditions. Such effects were less pronounced in the L-LC^3 mortars, likely because the lower reactivity of the calcined clay resulted in a filler-dominated behavior and a smaller impact on pore solution chemistry [32, 33].

Moreover, the decrease in potential observed in the H-LC^3 mortars prior to cracking may be associated with electrochemical transitions accompanying steel depassivation and the onset of active corrosion, including changes in local pore solution chemistry that increase its conductivity. This effect became more evident in the H-LC^3 mortars due to their substantially higher initial potential, whereas in the other systems such electrochemical transitions may be masked by their lower baseline potential.

After the gradual decreases in the potential curves of the H-LC^3 specimens, sharper drops were observed, as highlighted by the red perimeter in Fig. 6c These second sharper drops were evaluated as surface cracking, further corroborated by visual observations of corrosion products flowing out of openings on the sides of the specimens into the NaCl solution one to two days after the drop in electrical potential was detected.

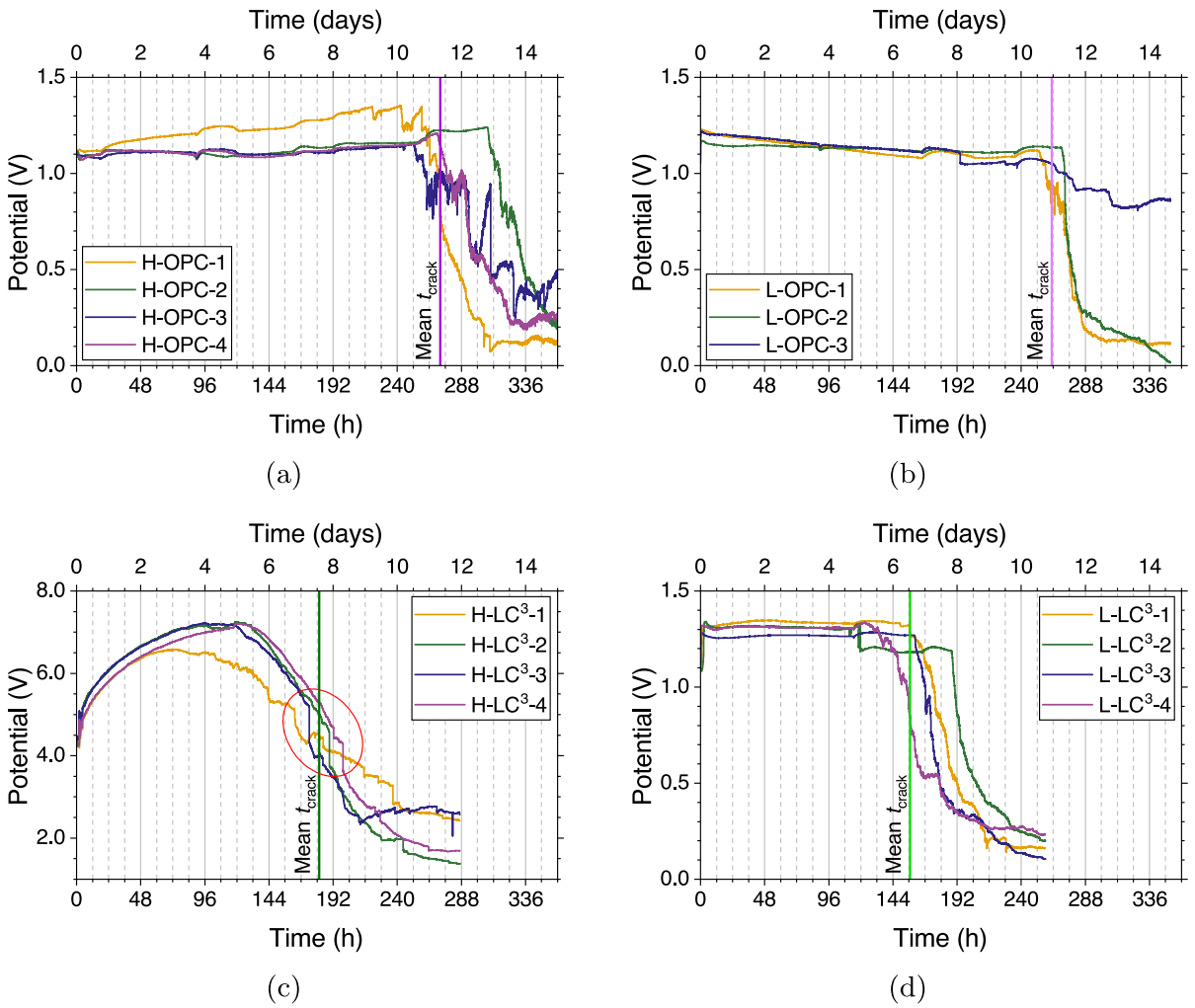

Fig. 6 Electrical potential U evolution during the impressed current corrosion test for **a** H-OPC, **b** L-OPC, **c** H-LC^3, and **d** L-LC^3 specimens. The time-to-cracking t_{crack} is identified by a sharp drop in potential. Vertical lines indicate the mean t_{crack} value for each mortar. Note that the scales on the y-axes differ

Table 2 Time-to-cracking t_{crack} values determined from electrical potential U measurements during the impressed current corrosion test

Mortar	t_{crack} (h)	t_{crack} (days)
H-OPC	272.1 ± 21.4	11.3 ± 0.9
L-OPC	262.9 ± 7.2	10.9 ± 0.3
H-LC^3	181.6 ± 13.9	7.6 ± 0.6
L-LC^3	156.9 ± 22.8	6.5 ± 0.9

Values are given as mean ± standard deviation

3.3 Correlation between t_{crack} and material properties

To investigate which material properties have the most influence on corrosion-induced cracking, t_{crack} was independently correlated with each property. The resulting relationships are shown in Fig. 9.

First, t_{crack} was correlated with the compressive strength f_c (Fig. 9a). No clear relationship was observed, as indicated by the low coefficient of determination obtained from a linear fit ($R^2 = 0.1005$). This outcome is expected, since corrosion-induced cracking is governed by splitting stresses generated by the volumetric expansion of corrosion products, rather than by compressive stresses acting on the mortar cover.

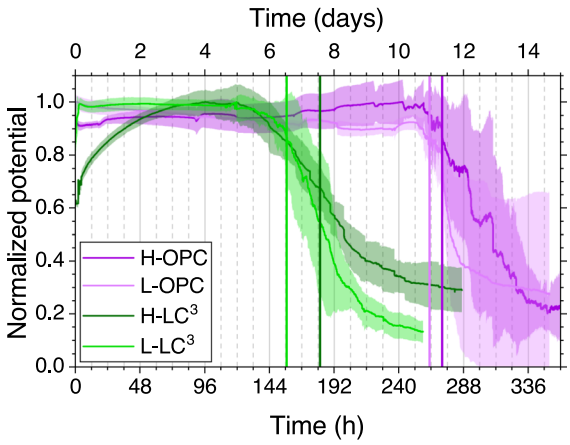

Fig. 7 Averaged and normalized electrical potential U of the different mortars during the corrosion experiment. Shaded regions represent the standard deviation, and vertical lines indicate the mean time-to-cracking t_{crack} for each color-corresponding mortar

Fig. 8 Final state of specimen L-LC^3-4 after the corrosion experiment, showing corrosion products emerging through a radial crack that reached the side of the specimen

A similar lack of correlation was observed between t_{crack} and the tensile strength f_t (Fig. 9b), for which the linear fit yielded a coefficient of determination $R^2 = 0.3159$. Although the expansion of corrosion products can induce tensile stresses in the surrounding mortar, these results suggest that tensile strength alone does not control the corrosion level required to initiate surface cracking.

In contrast, a strong correlation was observed between t_{crack} and the fracture energy G_F, as shown in Fig. 9c. A linear fit resulted in a high coefficient of determination ($R^2 = 0.9149$), indicating that mortars with a greater capacity to dissipate energy during crack propagation require a higher corrosion level to develop surface cracks. It should be noted that the G_F value of the H-LC^3 mortar was likely overestimated due to the post-peak behavior of the F_S-CMOD curve, as discussed in Sect. 3.1.3. Accounting for this overestimation would be expected to further strengthen the observed correlation, as indicated by the down arrow in Fig. 9c. Nonetheless, it is important to note that, since only four mortar compositions were investigated, the observed trend should be interpreted as an indication of a strong association rather than a universal law. Additional binder systems covering a broader range of fracture properties and behavior would be required to establish a general predictive relationship.

Finally, t_{crack} was correlated with the chloride migration coefficient D_{nssm} (Fig. 9d). The resulting linear fit yielded a coefficient of determination of $R^2 = 0.7129$, which is higher than those obtained for f_c and f_t, but still does not indicate a strong correlation with t_{crack}. This suggests that, although D_{nssm} is a useful indicator of pre-corrosion durability, it is not strongly related to corrosion cracking behavior.

4 Discussion

The present study highlights the complex interplay between mechanical behavior, transport properties, and corrosion-induced cracking in OPC- and LC^3-based cementitious mortars. On the one hand, LC^3-based mortars exhibited comparable mechanical performance and a clearly improved resistance to chloride transport compared to OPC systems. On the other hand, OPC mortars showed superior performance with respect to fracture-related mechanisms activated under splitting loading and corrosion-induced expansion, as evidenced by the wedge splitting and impressed current corrosion tests. This contrast emphasizes the importance of fracture energy as a governing property for corrosion-induced cracking, a relationship that is often overlooked in performance assessments of new binders, relying primarily

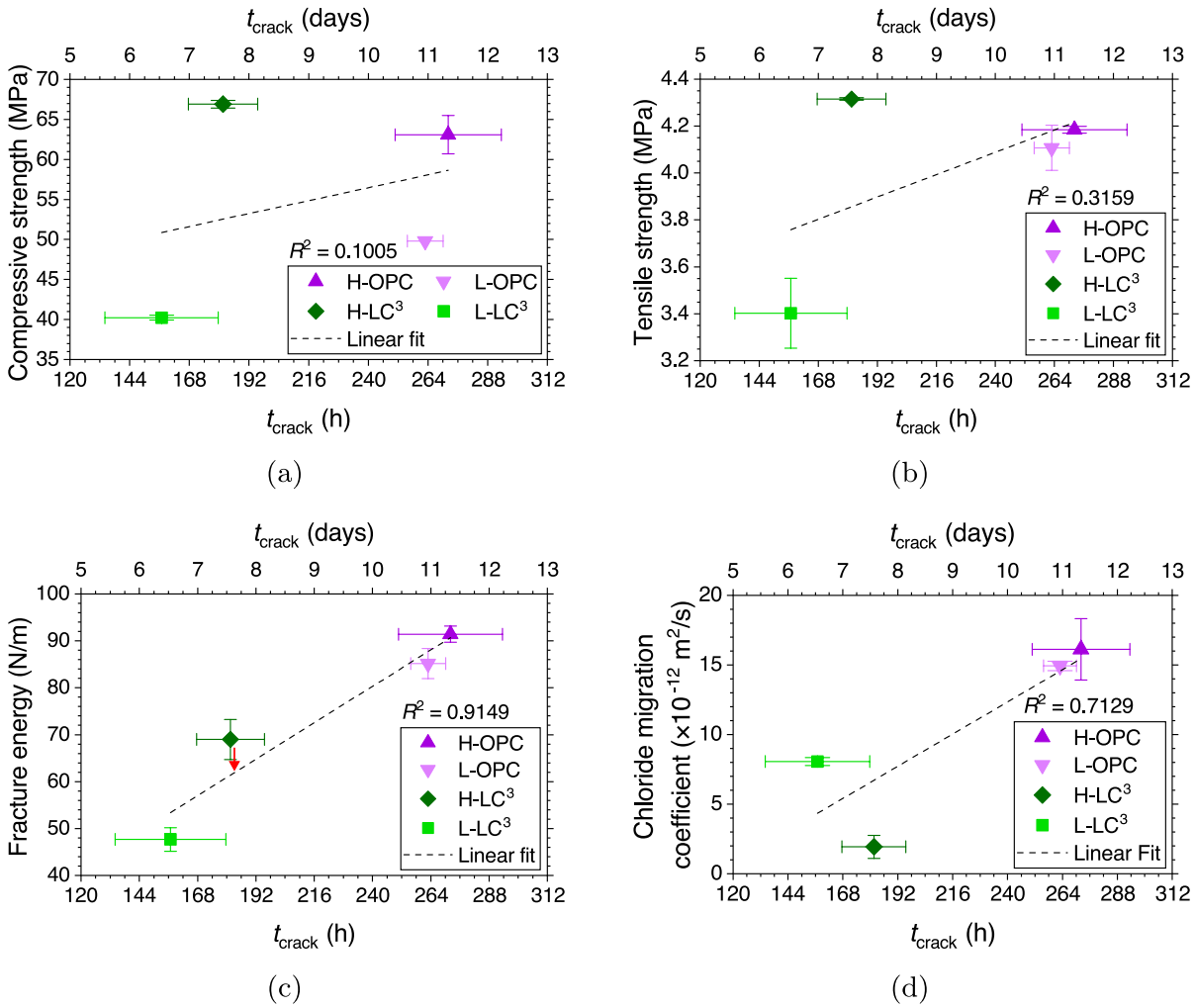

Fig. 9 Correlation between the time-to-cracking t_{crack} and selected material properties: **a** compressive strength f_c, **b** tensile strength f_t, **c** fracture energy G_F, and **d** chloride migration coefficient D_{nssm}. Dashed lines represent linear fits, and the corresponding coefficients of determination R^2 are indicated in each plot. In (**c**), the down arrow indicates the expected shift of the H-LC^3 data point due to the likely overestimation of G_F

on strength and transport indicators, which may not adequately capture post-cracking behavior.

Among the measured properties, chloride migration coefficient and fracture energy were found to be particularly sensitive to the binder type. Previous studies have shown that cementitious systems incorporating kaolinitic clays, such as LC^3 binders, promote pore refinement, leading to improvements in several durability-related indicators, including a reduced chloride migration coefficient [14, 27, 30]. A similar reduction in chloride migration was observed in the present study, indicating that LC^3 mortars offer enhanced resistance to chloride ingress, most likely due to their finer pore structure. This characteristic can significantly contribute to durability with respect to steel reinforcement corrosion by delaying the transport of chloride ions to the steel-concrete interface and, consequently, the depassivation of the protective oxide layer.

However, the same pore refinement that improves transport resistance may adversely affect the fracture behavior of LC^3 mortars. The densification

of the cementitious matrix induced by SCMs can hinder crack initiation, but once cracking occurs, fracture may proceed in a more abrupt manner due to a reduced post-peak fracture process zone and increased brittleness [34]. This behavior was particularly evident in the H-LC^3 mortar. In addition, previous studies have shown that the incorporation of SCMs can strengthen the interfacial transition zone (ITZ), promoting crack propagation through aggregates rather than along the paste-aggregate interface and thereby increasing fracture toughness [35]. Furthermore, improvements in ITZ properties may continue at increased curing ages due to the slower pozzolanic reactions associated with calcined clays [36]. Since all mortars in this study were tested at approximately 28 days and the investigation was limited to mortar-scale specimens, further research is needed to evaluate how longer curing times and concrete-scale heterogeneity influence the fracture performance of LC^3-based systems. It is worth noting that fracture energy can also be enhanced by increasing aggregate size [37]. However, the present study was limited to mortars with a maximum aggregate size of 4 mm.

The reduced fracture performance of LC^3 mortars had a direct impact on their resistance to corrosion-induced cracking. As shown in Fig. 9c. This finding indicates that fracture energy is a relevant factor for assessing the ability of cementitious materials to withstand splitting stresses generated by the expansion of corrosion products during the propagation stage of reinforcement corrosion. Consequently, mortars with lower fracture energy, such as the LC^3-based systems investigated here, cracked at lower corrosion levels than the OPC mortars. This behavior is not necessarily unfavorable, since corrosion-induced cracking at lower corrosion levels may act as an early indicator of deterioration before significant reinforcement cross-sectional loss occurs, allowing for earlier maintenance actions. Nevertheless, earlier cracking can also lead to faster propagation of spalling if timely intervention is not undertaken.

Finally, while LC^3 mortars exhibited corrosion-induced cracking at lower corrosion levels, this relative limitation may be partially offset by their enhanced resistance to chloride ingress, which delays corrosion initiation. However, the influence of these competing mechanisms on the overall service life of steel-reinforced concrete structures should be further assessed under natural corrosion conditions. Moreover, it should be noted that concrete structures are often already cracked due to external loading, creep, shrinkage, or restraint effects. Such cracks can act as preferential pathways for chloride ingress, potentially accelerating corrosion initiation even in dense cementitious matrices, such as those produced with LC^3. Therefore, although fracture energy was found to be closely related to t_{crack} in this study and shows promise as a parameter for predicting long-term performance during corrosion propagation, further research is required to account for the combined effects of cracking, transport, material aging, and structural loading conditions.

5 Conclusions

In this work, the influence of binder type and material properties on the performance of steel-reinforced mortars with Limestone Calcined Clay Cement (LC^3) and Ordinary Portland Cement (OPC) against corrosion-induced cracking was investigated. For each binder type, a higher-strength mortar (H-OPC and H-LC^3) and a lower-strength mortar (L-OPC and L-LC^3) were studied.

The main findings can be summarized as follows:

- Mortars produced with either OPC or LC^3 that were optimized for comparable strengths show a large variation in the fracture properties, hence resistance to corrosion-induced cracking, implying that binder design leads to larger differences in fracture energy than conventional strength metrics.
- Despite having comparable or higher compressive and tensile strengths, LC^3 mortars exhibited lower fracture energy and a more brittle response compared to OPC mortars, particularly in the case of H-LC^3.
- LC^3 mortars reached surface cracking at lower corrosion levels compared to OPC mortars.
- Fracture energy showed a strong correlation with the corrosion level causing cracking, indicating that it is a relevant property for describing corrosion-induced damage during the propagation stage.

Overall, these findings highlight a trade-off between resistance to corrosion initiation, assessed here and in previous studies through the substantially higher

resistance to chloride ingress of LC^3 mortars, and resistance to corrosion propagation. Therefore, the durability assessment of steel-reinforced cementitious systems may benefit from considering both transport- and fracture-related properties upon further assessment of this trade-off under natural corrosion conditions. From a structural safety perspective, this trade-off may also have practical implications. On the one hand, earlier corrosion-induced cracking could provide visible indicators of deterioration before significant loss of reinforcement cross-sectional area occurs. In contrast, it may also accelerate the propagation of spalling, compromising even further the long-term performance of steel-reinforced concrete structures.

Acknowledgements The authors gratefully acknowledge the Wallenberg Initiative Materials Science for Sustainability (WISE), funded by the Knut and Alice Wallenberg Foundation, for supporting this research.

Funding Open access funding provided by Chalmers University of Technology. Open access funding provided by Chalmers University of Technology.

Data availability Data sets generated during the current study are available from the corresponding author on reasonable request.

Declarations

Conflict of interest The authors declare that they have no conflict of interest.

References

1. Snellings R, Suraneni P, Skibsted J (2023) Future and emerging supplementary cementitious materials. Cem Concr Res 171:107199. https://doi.org/10.1016/j.cemconres.2023.107199
2. Alujas Diaz A, Almenares Reyes RS, Hanein T et al (2022) Properties and occurrence of clay resources for use as supplementary cementitious materials: a paper of RILEM TC 282-CCL. Mater Struct 55(5):139. https://doi.org/10.1617/s11527-022-01972-2
3. Antoni M, Rossen J, Martirena F et al (2012) Cement substitution by a combination of metakaolin and limestone. Cem Concr Res 42(12):1579–1589. https://doi.org/10.1016/j.cemconres.2012.09.006
4. Tang J, Ma SH, Li WF, et al (2021) Research progress on the hydration of portland cement with calcined clay and limestone. In: Materials in machinery and construction, materials science forum, vol 1036. Trans Tech Publications Ltd, pp 240–246. https://doi.org/10.4028/www.scientific.net/MSF.1036.240
5. Parashar A, Bishnoi S (2021) Hydration behaviour of limestone-calcined clay and limestone-slag blends in ternary cement. RILEM Tech Lett 6:17–24. https://doi.org/10.21809/rilemtechlett.2021.134
6. Jiang J, Sui S, Liu Z et al (2025) Research on silicoaluminate-based low-carbon cementitious material—a state-of-the-art review. Fundam Res 5(6):2799–2814. https://doi.org/10.1016/j.fmre.2024.04.020
7. Scrivener K, Martirena F, Bishnoi S et al (2018) Calcined clay limestone cements (LC^3). Cem Concr Res 114:49–56. https://doi.org/10.1016/j.cemconres.2017.08.017
8. Sharma M, Bishnoi S, Martirena F et al (2021) Limestone calcined clay cement and concrete: a state-of-the-art review. Cem Concr Res 149:106564. https://doi.org/10.1016/j.cemconres.2021.106564
9. Gettu R, Patel A, Rathi V et al (2019) Influence of supplementary cementitious materials on the sustainability parameters of cements and concretes in the Indian context. Mater Struct 52(1):10. https://doi.org/10.1617/s11527-019-1321-5
10. Poursaee A, Hansson C (2009) Potential pitfalls in assessing chloride-induced corrosion of steel in concrete. Cem Concr Res 39(5):391–400. https://doi.org/10.1016/j.cemconres.2009.01.015
11. Papadakis VG (2000) Effect of supplementary cementing materials on concrete resistance against carbonation and chloride ingress. Cem Concr Res 30(2):291–299. https://doi.org/10.1016/S0008-8846(99)00249-5
12. Thomas MDA (2019) Durability of concrete. In: Thomas MDA (ed) Supplementary cementing materials in concrete. CRC Press, Boca Raton, FL, chap 9, p 151–208. https://doi.org/10.1201/b14493-9
13. Dhandapani Y, Sakthivel T, Santhanam M et al (2018) Mechanical properties and durability performance of concretes with Limestone calcined clay cement (LC^3). Cem Concr Res 107:136–151. https://doi.org/10.1016/j.cemconres.2018.02.005
14. Dhandapani Y, Machner A, Wilson W et al (2024) Performance of cementitious systems containing calcined clay in a chloride-rich environment: a review by TC-282 CCL. Mater Struct 57:154. https://doi.org/10.1617/s11527-024-02426-7
15. Wang HL, Dai JG, Sun XY et al (2016) Characteristics of concrete cracks and their influence on chloride penetration. Construct Build Mater 107:216–225. https://doi.org/10.1016/j.conbuildmat.2016.01.002

16. Djerbi A, Bonnet S, Khelidj A et al (2008) Influence of traversing crack on chloride diffusion into concrete. Cem Concr Res 38(6):877–883. https://doi.org/10.1016/j.cemconres.2007.10.007
17. Wang X, Ba M, Yi B et al (2024) Experimental and numerical investigation on the effect of cracks on chloride diffusion and steel corrosion in concrete. J Build Eng 86:108521. https://doi.org/10.1016/j.jobe.2024.108521
18. Bertolini L, Elsener B, Pedeferri P et al (2013) Corrosion of steel in concrete —prevention, diagnosis, repair (2nd Edition). John Wiley & Sons, Weinheim, Germany. https://doi.org/10.1002/9783527651696
19. Brühwiler E, Wittmann FH (1990) The wedge splitting test, a new method of performing stable fracture mechanics tests. Eng Fract Mech 35(1):117–125. https://doi.org/10.1016/0013-7944(90)90189-N. (**Special Issue Fracture and Damage of Concrete and Rock**)
20. Cheng L, Kurihara R, Ohkubo T et al (2024) Plugging effect of fine pore water in OPC and LC^3 paste during accelerated carbonation monitored via single-sided nuclear magnetic resonance spectroscopy. Cem Concr Res 186:107688. https://doi.org/10.1016/J.CEMCONRES.2024.107688
21. Feng W, Tarakbay A, Ali Memon S et al (2021) Methods of accelerating chloride-induced corrosion in steel-reinforced concrete: a comparative review. Construct Build Mater 289:123165. https://doi.org/10.1016/j.conbuildmat.2021.123165
22. Shi J, Ming J, Sun W (2018) Accelerated corrosion behavior of steel in concrete subjected to sustained flexural loading using electrochemical methods and X-Ray computed tomography. J Mater Civ Eng 30(7):04018131. https://doi.org/10.1061/(ASCE)MT.1943-5533.0002337
23. Alonso C, Andrade C, Rodriguez J et al (1998) Factors controlling cracking of concrete affected by reinforcement corrosion. Mater Struct 31(7):435–441. https://doi.org/10.1007/BF02480466
24. Alhede A, Dijkstra J, Tengattini A et al (2025) Characterisation of steel corrosion and matrix damage in reinforced mortar combining analytical, electrical and image-based techniques. Cem Concr Res 190:107792. https://doi.org/10.1016/j.cemconres.2025.107792
25. European Committee for Standardization (2019) EN 12390–3: Testing hardened concrete - Part 3: Compressive strength of test specimens. Tech. rep, CEN, Brussels, Belgium
26. NORDTEST (1999) NT BUILD 492: Concrete, mortar and cement-based repair materials: chloride migration coefficient from non-steady-state migration experiments. Tech. rep, NORDTEST, Espoo, Finland
27. Avet F, Scrivener K (2018) Investigation of the calcined kaolinite content on the hydration of Limestone calcined clay cement (LC^3). Cem Concr Res 107:124–135. https://doi.org/10.1016/j.cemconres.2018.02.016
28. Maraghechi H, Avet F, Wong H et al (2018) Performance of Limestone Calcined Clay Cement (LC^3) with various kaolinite contents with respect to chloride transport. Mater Struct 51(5):125. https://doi.org/10.1617/s11527-018-1255-3
29. Wang Y, Miao X, Zhao Y et al (2024b) Quantitative image analysis on the filling proportion of corrosion products in reinforced concrete using X-ray computed tomography. Cem Concr Compos 150:105558. j.cemconcomp.2024.105558
30. Dhandapani Y, Santhanam M (2017) Assessment of pore structure evolution in the limestone calcined clay cementitious system and its implications for performance. Cem Concr Compos 84:36–47. https://doi.org/10.1016/j.cemconcomp.2017.08.012
31. Rengaraju S, Pillai RG (2023) Long-term corrosion performance and monitoring for service life estimation of LC3 concrete systems. Mater Struct 12:1592–1603. https://doi.org/10.1080/21650373.2023.2246068
32. Wilson W, Georget F, Scrivener K (2021) Unravelling chloride transport/microstructure relationships for blended-cement pastes with the mini-migration method. Cem Concr Res 140:106264. https://doi.org/10.1016/j.cemconres.2020.106264
33. Wilson W, Georget F, Scrivener KL (2024) Towards a two-step assessment of the chloride ingress behaviour of new cementitious binders. Cem Concr Res 184:107594. https://doi.org/10.1016/j.cemconres.2024.107594
34. Molaei Raisi E, Vaseghi Amiri J, Davoodi MR (2018) Influence of rice husk ash on the fracture characteristics and brittleness of self-compacting concrete. Eng Fract Mech 199:595–608. https://doi.org/10.1016/j.engfracmech.2018.06.025
35. Kumar A, Singh GJ, Chauhan BL et al (2024) Strength and durability performance of recycled aggregate structural concrete with silica fume, furnace slag, and m-fine. J Mater Civ Eng 36:04024165. https://doi.org/10.1061/jmcee7.mteng-17547
36. Duan P, Shui Z, Chen W et al (2013) Efficiency of mineral admixtures in concrete: microstructure, compressive strength and stability of hydrate phases. Appl Clay Sci 83–84:115–121. https://doi.org/10.1016/j.clay.2013.08.021
37. Khalilpour S, BaniAsad E, Dehestani M (2019) A review on concrete fracture energy and effective parameters. Cem Concr Res 120:294–321. https://doi.org/10.1016/j.cemconres.2019.03.013
38. European Committee for Standardization (2011) EN 197–1: Cement - Part 1: Composition, specifications and conformity criteria for common cement. Tech. rep, CEN, Brussels, Belgium